Field-Modulation Imaging of Ferroelectric Domains in Molecular Single-Crystal Films

Yohei Uemura, Shunto Arai, Jun'ya Tsutsumi, Satoshi Matsuoka, Hiroyuki Yamada, Reiji Kumai, Sachio Horiuchi, Akihito Sawa, and Tatsuo Hasegawa

Phys. Rev. Applied **11**, 014046 — Published 23 January 2019

DOI: 10.1103/PhysRevApplied.11.014046

Field Modulation Imaging of Ferroelectric Domains in Molecular Single-Crystal Film

Yohei Uemura[1, *], Shunto Arai[1], Jun'ya Tsutsumi[2], Satoshi Matsuoka[1], Hiroyuki Yamada[3], Reiji Kumai[4], Sachio Horiuchi[2], Akihito Sawa[3], Tatsuo Hasegawa[1,2, †]

[1]*Department of Applied Physics, The University of Tokyo, Tokyo 113-8656, Japan*
[2]*Flexible Electronics Research Center (FLEC), National Institute of Advanced Industrial Science and Technology (AIST), Tsukuba, Ibaraki 305-8565, Japan*
[3]*Electronics and Photonics Research Institute (ESPRIT), National Institute of Advanced Industrial Science and Technology (AIST), Tsukuba, Ibaraki 305-8565, Japan*
[4]*Condensed Matter Research Center (CMRC) and Photon Factory, Institute of Materials Structure Science, High Energy Accelerator Research Organization (KEK), Tsukuba 305-0801, Japan*

Many hydrogen-bonded organic ferroelectrics exhibit low-field switching of large spontaneous polarizations. Although the switchable electric dipoles of π-conjugated organic molecules account for the large spontaneous polarizations, their relevant optoelectronic processes have not been used to probe the ferroelectricity. Here, we show that the variation in electro-optic response enables visualization of the ferroelectric domains and domain walls in single-crystal films of a hydrogen-bonded molecular co-crystal. Highly sensitive and rapid visualization is realized by difference optical image sensing between the forward and reverse field applications. We call this technique "ferroelectrics field modulation imaging (FFMI)." The unique optical-probe nature reveals the existence of two types of domain walls showing different three-dimensional orientations within the films; one is roughly perpendicular to the film plane, whereas the other is considerably tilted from the normal to the plane. We discuss that both of the domain walls are stabilized to generate substantial neutrality by being directed parallel to the direction of polarization. This study opens a new route for exploring the three-dimensional topological nature of domain walls in ferroelectric materials.

I. INTRODUCTION

Ferroelectrics are usually composed of multiple domain walls that separate domains of different polarization orientations and strongly affect the switching properties. To understand the ferroelectric switching characteristics, it is essential to clarify how the domain walls emerge, move, merge, and disappear within the crystals [1–4]. Basically, the domain walls are classified into two categories: charged domain walls that have a bound charge, and neutral domain walls that do not have a bound charge. The charged domain walls are expected to have much higher generation energy and lower mobility than the neutral domain walls because of the presence of the bound charges, which may affect (or deteriorate) the ferroelectric switching characteristics [5]. However, it is also pointed out that the domain wall motions are strongly coupled with lattice elastic energy in inorganic (perovskite-type) ferroelectrics [6, 7]. Accordingly, it is difficult to discriminate the effects of the bound charge and lattice elastic energy, leading to controversy over their influence on switching characteristics. An ideal ferroelectric system without the lattice deformation coupling and the characteristics of domain walls have not been fully investigated and clarified.

The proton-transfer-type organic ferroelectrics are a novel class of ferroelectric materials composed of π-conjugated molecules that are linked by hydrogen bonding [8–10]. The lattice elastic energy in these materials is negligible because spontaneous polarization originates from the cooperative transfer of protons within the crystals as well as from the electric dipoles of π-conjugated organic molecules [11, 12]. Tactical design of the molecular materials with use of hydrogen bonding allows to reverse the crystal symmetry with cooperative proton transfer and least change in the structures of host molecular moieties. This strategy demands pseudo-symmetric elements on the host moieties from the crystallographic viewpoint. In fact, many of the materials present room-temperature ferroelectricity with a much lower coercive

field (10–20 kV/cm) than that of ferroelectric polymers, which exceeds 500 kV/cm [13, 14]. The soluble, lead-free, and rare-metals-free characteristics suggest that these are promising materials to be used for printed electronics devices operating at low voltages [15, 16].

For the observation of ferroelectric domains and domain walls, various non-destructive techniques have been developed, such as piezoresponse force microscopy (PFM) [17, 18], scanning nonlinear dielectric microscopy (SNDM) [19, 20], polarization microscopy [1], second harmonic generation (SHG) microscopy [21, 22], and terahertz radiation imaging [23, 24]. Another technique being studied is based on slight responses of the optical spectrum of a ferroelectric charge-transfer (CT) complex under external electric fields [25]. The technique is based on a first-order electro-absorption (i.e., the Pockels) effect for ferroelectric materials that do not have inversion symmetry. It utilizes the slight reflectance changes under an electric field at respective positions to visualize ferroelectric domain structures. It takes advantage of the relatively large optical response of organic CT complex to the external electric field. Nevertheless, the technique has not yet been applied to other ferroelectric materials, including the proton-transfer-type organic ferroelectrics, primarily because a long measurement time is required for the two-dimensional scanning of the entire target area where the slight optical response must be measured by a lock-in technique at the respective positions.

In this study, we visualize the ferroelectric domains and domain walls within single-crystal films of proton-transfer-type organic ferroelectrics, based on the slight changes in optical absorption induced by an applied electric field. For this purpose, we apply a difference image sensing technique using a CMOS area image sensor, which enabled highly sensitive, collective, and quick detection of tiny changes in optical transmittance in the order of 10^{-4}. As the ferroelectric material, we choose proton-transferred salt of chloranilic acid (H_2ca) and 2,3-di(2-pyridinyl)pyrazine (dppz), denoted as Hdppz-Hca, which is soluble in

organic solvent and exhibits excellent ferroelectric characteristics at room temperature (T_c = 402 K) [10]. We demonstrate that the FFMI technique, developed in this study, permits the rapid acquisition of images of the ferroelectric domain structures within a few minutes, over a wide area as large as 1 mm^2, and at high spatial resolution as small as several hundred nm. Furthermore, we demonstrate that three-dimensional domain structures in the depth direction can be visualized within the films.

II. EXPERIMENT

A. Fabrication and characterization of ferroelectric thin films

The crystal structure of Hdppz-Hca is presented in Fig. 1(a). Acid molecules (H_2ca) and base molecules (dppz) are alternately linked by hydrogen bonds to form one-dimensional molecular chains along the *c*-axis in the crystal. The overall crystal structure has a pseudo-symmetry of space group *C*2/*c* (#15) by locating the deprotonated dppz and ca^{2-} moieties on the twofold axis and inversion symmetry, respectively. The asymmetric ordering of protons reduces the crystal symmetry to the actual space group *Cc* (#9), in which the spontaneous polarization is allowed within the *ac*-plane.

Single-crystal thin films of Hdppz-Hca were fabricated by using the confined crystal growth technique. Prior to the crystal growth, comb-shaped electrodes were fabricated on a glass plate by vacuum deposition. Another glass plate was coated with a highly hydrophobic fluorinated polymer layer by using the spin coating method. A solution of dppz and H_2ca in *N,N*-dimethylformamide was confined in a narrow space between the glass plate with the electrodes and the glass plate with the fluorinated polymer. After the slow evaporation of solvent and the crystal growth, the cover glass with the fluorinated polymer layer was detached from the glass plate with the film and the electrodes. Since the surface of fluorinated polymer is hydrophobic, crystals remained only on the glass substrate. As a result,

single-crystal thin films, with thickness ranging between 0.3 and 2 μm, were obtained over a number of electrodes. The line-and-space widths of the comb-shaped electrodes were L/S = 100/50 μm. The thickness of the electrodes was 32 nm (Cr: 2 nm, Au: 30 nm). The density of the solution was 1.5 wt%, and the amount of solution confined between the glass plate was 20 μL. The thickness profile of the films was measured by atomic force microscopy (MFP-3D in tapping mode; Asylum Research).

To investigate the crystallographic axes of the films, we conducted synchrotron-radiated X-ray diffraction measurements at the BL-8B line of the KEK (High Energy Accelerator Research Organization) Photon Factory. The x-rays had an energy of 18 keV, which was calibrated using CeO_2. Orientation of crystal axis was determined by out-of-plane and high-incident-angle diffractions using the analysis software (RAPID AUTO; Rigaku).

Conventional PFM measurements were conducted with a commercially available scanning probe microscope (MFP-3D; Asylum Research) using a conducting tip (PPP-NCSTPt-20; Nanosensors). Dual AC resonance tracking mode was used to suppress the noise. Comb-shaped electrodes under ferroelectric films were grounded via gold wires.

B. Electro-absorption spectroscopy

The ordinary optical absorption spectrum of Hdppz-Hca was measured by a spectrophotometer (UV-2450; Shimadzu). Hdppz-Hca thin films on the glass substrate were measured using transmitted light irradiated from the back side of the substrate.

The electro-absorption spectrum was measured by using the lock-in technique. Monochromatic light from a Xe lamp obtained through a spectroscope was focused onto a uniform polarization domain through a flare diaphragm, and the transmitted light was detected by photodiodes. Square-wave bias voltage was applied between the electrodes at a frequency of 45 Hz, and the difference between transmittance under positive (T_+) and negative (T_-) bias was measured by a lock-in amplifier, using the square-wave reference signal at 45 Hz. By

scanning the wavelength of the probe light, the modulation spectrum ($-\Delta T/T = -(T_+ - T_-)/T$) was obtained. The amplitude of the bias voltage was set at 20 $V_{p\text{-}p}$.

C. Field modulation imaging technique

Square-wave bias voltage was applied between the electrodes at a frequency of 45 Hz. The amplitude of the bias voltage was 20 $V_{p\text{-}p}$. Pulsed monochromatic light at a frequency of 90 Hz from an LED was irradiated onto the sample from the back side of the glass substrate, where the pulsed irradiation was synchronized with the applied square-wave bias voltage. The wavelength was 565 nm, and the pulse width was 1 ms. Transmitted light was captured by a CMOS area image sensor to obtain images at positive and negative bias, respectively. The difference between the positive-bias image and the negative-bias image is denoted by ΔT, and the average of the positive-bias image and the negative-bias image is denoted by T. $\Delta T/T$ was calculated for each pixel detection and the spatial distribution of $\Delta T/T$ was obtained, which visualizes the ferroelectric domain structures. To suppress the noise, 16,384 images were captured for the positive- and negative-bias states, respectively, and were averaged.

The dynamics of the ferroelectric domain wall motion were driven by applying a large static voltage (100 V) between the electrodes. Then the FFMI image was measured by applying a small modulation voltage (20 $V_{p\text{-}p}$). Driving of the domain wall motion and measurement of the FFMI were conducted alternately. The large static voltage was turned off during the FFMI measurements.

III. RESULTS AND DISCUSSIONS

A. Ferroelectrics field-modulation imaging based on electro-absorption effect

An example of the sensitive optical response of the π-conjugated electrons to the protonation (or deprotonation) was demonstrated by the absorption spectra of the component

molecules of Hdppz-Hca in solution. Figure 1(b) shows the molar absorption spectra of neutral H_2ca, ionic Hca^-, and divalent ca^{2-} in acetonitrile solution [26]. It is seen that the Hca^- ions exhibit much larger absorbance than that of H_2ca and ca^{2-} in the visible range. The plot indicates that the electronic absorption of Hca^- ions in Hddpz-Hca depends considerably on the degree of intermolecular proton transfer. The changes in optical response of Hdppz-Hca under external electric fields will tell us how the proton locations are modulated. Note that the spectral change in the visible range is not relevant to the absorption band of $Hdppz^+$, which appears only in the ultraviolet range at around 4.35 eV [27].

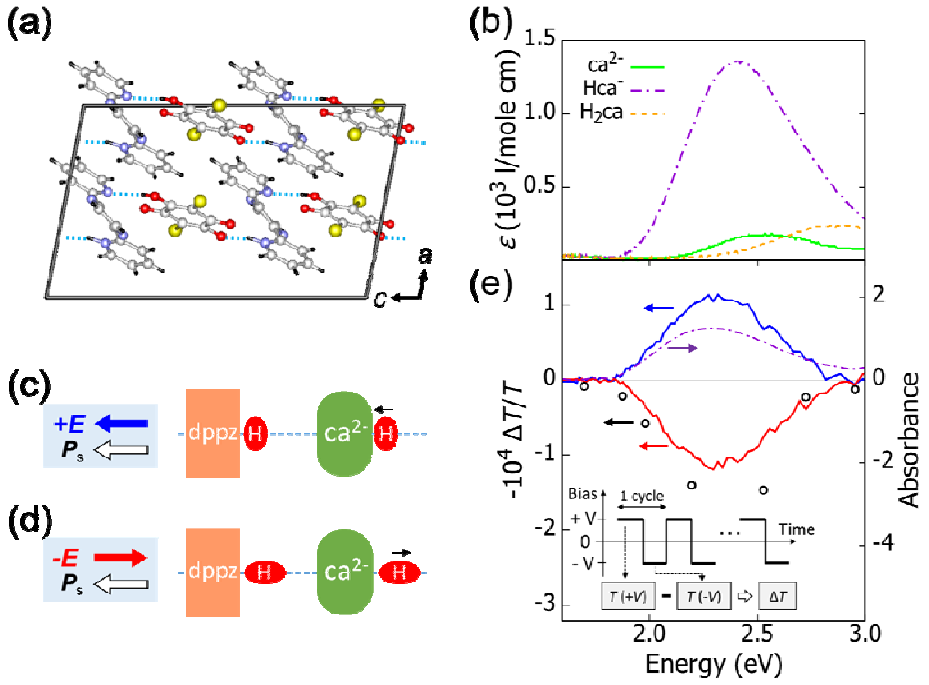

FIG. 1. Hydrogen-bonded organic ferroelectric, Hdppz-Hca, and its optical response. (a) Crystal structure of Hdppz-Hca. Hydrogen-bonded chains are along the *c*-axis. (b) Molar absorption spectra of chloranilic acid in acetonitrile solution at different protonation states; neutral H_2ca, deprotonated Hca^- monoanion, and ca^{2-} dianion. Reproduced with permission (R. Kumai, *et al., J. Chem. Phys.* **125,** 084715 (2006).) [26]. (c), (d) Schematic of proton displacement under external electric fields. When the field is applied along the direction of the spontaneous polarization, the protons move closer to ca^{2-}, which is expected to increase the absorbance (c). When the field is applied opposite to the spontaneous polarization, the protons

move further away from ca^{2-}, which is expected to decrease the absorbance (d). (e) Electro-absorption spectrum of Hdppz-Hca film. The blue and red curves are the field modulation spectra obtained for a ferroelectric domain, at the initial ferroelectric state and after the polarization reversal, respectively. The dashed curve is the normal absorbance spectrum. Black open circles are the average FFMI signal intensity obtained at each photon energy (see Supplementary Fig. S4 [28]).

To sensitively detect the change in local transmittance, we applied an alternating electric field over a single-crystal film by using a pair of counter electrodes (see Supplementary Fig. S1 [28]). Note that the *bc*-plane of the single-crystal film is parallel to the substrate surface, as presented in Fig. 1(a). The transmittance under positive (T_+) and negative bias (T_-) was detected, collectively, by an area image sensor, as schematically shown in Fig. 2(a). The obtained difference image ($\Delta T = T_+ - T_-$) for the as-grown film is presented in Fig. 2(b). The positive (red) and negative (blue) signals indicate the increase and decrease in transmittance, respectively, under the applied positive bias. Figure 2(c) shows the lateral PFM phase image obtained over the same area as in Fig. 2(b). The FFMI image is highly consistent with the PFM image, confirming that the FFMI enables visualization of the ferroelectric domain structures. We also confirm that the modulation bias does not affect the ferroelectric domain structures, as shown in Supplementary Fig. S2 [28]. Note that the FFMI technique was created based on the gate-modulation imaging (GMI) technique that was recently developed to visualize carrier density within the channel layers of organic thin-film transistors [29]. The FFMI is advantageous compared to PFM because it is possible to visualize the entire domain structures over a wide area, rapidly, and at high resolution, simultaneously (see Supplementary Fig. S3 [28]).

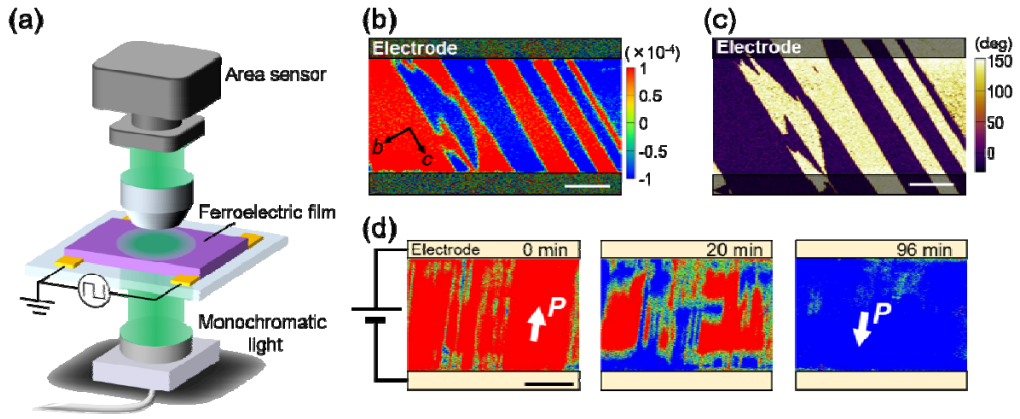

FIG. 2. Ferroelectrics field modulation imaging, FFMI, and typical obtained images. (a) Schematic representation of the FFMI measurement. (b) Typical FFMI image of Hdppz-Hca single-crystal film. (c) Lateral PFM phase image of the same area as (b). Same ferroelectric domains and domain walls are clearly identified in (b) and (c). (d) FFMI images of Hdppz-Hca single-crystal film, measured at the initial ferroelectric state (left), and at 20 min (centre) and 96 min (right) after the application of an external electric field of 20 kV/cm. Domain wall motions are clearly observed during the polarization reversal. White arrows depict the horizontal component of spontaneous polarization. Scale bar is 20 μm.

To investigate the origin of the modulation signal in the FFMI, we measured the first-order electro-absorption spectra of Hdppz-Hca. The spectra of the ferroelectric domains, reversed with each other, are shown by the blue and red curves in Fig. 1(e), respectively. Both spectra present similar features, except for the sign of the signal, with the original absorption spectrum as shown by the dashed curve. Also plotted in Fig. 1(e) is the FFMI signal measured at various photon energies (all the images are shown in Supplementary Fig. S4 [28]), which is consistent with the electro-absorption spectra. The results indicate that the absorption is simply increased or decreased by the application of external electric fields, which is consistent with the assumption that the slight displacement of protons by applied electric fields causes the change in optical transmittance or absorbance. We estimate that about 0.01% of the absorbance is modulated by an external electric field of ±2 kV/cm: when electric field is applied along the same (opposite) direction as spontaneous polarization $\boldsymbol{P}_s$ as $\boldsymbol{E} \cdot \boldsymbol{P}_s > 0$ ($\boldsymbol{E} \cdot \boldsymbol{P}_s$

< 0), the protons move closer to (farther from) the ca^{2-} molecule, so that the absorption of Hca^{-} ions increases (decreases) (Fig. 1(c), (d)).

We now discuss the switching behaviour of ferroelectric domains based on the observed FFMI images. Figure 2(d) presents FFMI images before and after the application of external electric field $\boldsymbol{E}$ that exceeds the coercive field E_c ($|\boldsymbol{E}| > E_c$). A gradual change of domains through the motion of domain walls is observed (see also Supplementary Fig. S5 [28]). These observations demonstrate that the polarization reversal within the films takes about 90 min, which is much slower than that in bulk crystals in which polarization switches at a higher frequency than 1 kHz. It is also found that almost no change is observed in the domain structures before and after the application of static electric field of 5 kV/cm, which is larger than coercive electric field of bulk crystal (< 2 kV/cm) (see also Supplementary Fig. S6 [28]). These results indicate that the coercive electric field of the single-crystal film is much larger than that of bulk crystal. This feature should be ascribed to the pinning of domain walls at the film/substrate and film/air interfaces, or to the disappearance of ferroelectricity at the film/electrode interface [30–32].

B. Internal structure of ferroelectric domain walls

In the FFMI image acquired during the process of polarization reversal (Fig. 2(d), center), we notice that the intensity variation of the FFMI signal is fairly gradual at around the domain boundaries. In addition, the spatial width of this gradual change crucially depends on the direction of the domain walls. Figure 3(a) shows an enlarged view of the image around the domain walls measured just after the local colour changes from red to blue due to the domain wall motion along the white-arrow direction by applying the electric field. The domain boundaries that are parallel to the *c*-axis (or parallel to the hydrogen-bonded chains) exhibit rapid changes in the FFMI signal across the axis perpendicular to the boundaries. In contrast,

the domain boundaries that are roughly perpendicular to the *c*-axis (and parallel to the *b*-axis) have a large spatial width for the signal variation. Here, we call the former domain walls DW1, and the latter DW2. We note that DW1 and DW2 seem to be the neutral and charged domain walls, respectively, considering that DW2 is perpendicular to the hydrogen-bonded chains in the PFM image. However, we found that this was not the case, as described later.

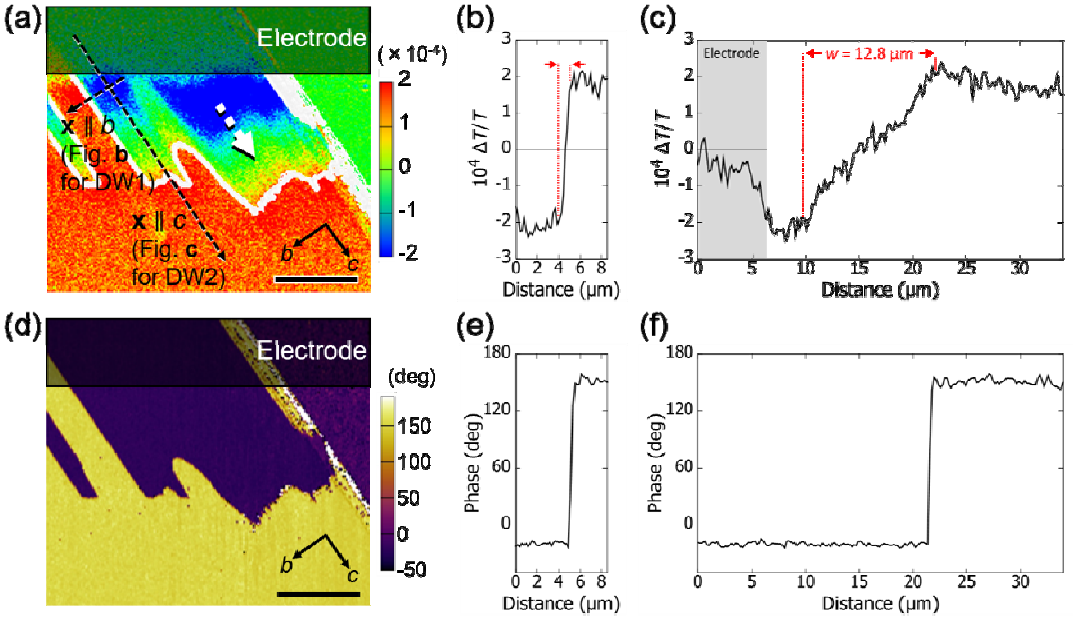

FIG. 3. Comparison of FFMI image and PFM phase image around the domain walls. (a) Typical FFMI image of Hdppz-Hca single-crystal film around the domain wall, which is moved along the direction shown by the white dotted arrow. White curve in the image indicates the domain wall as observed by the lateral PFM phase image (d). (b), (c) Variation of FFMI signal intensity as a function of the film position, across DW1 (***x*** *b*) (b) and across DW2 (***x*** *c*) (c), along the black dashed arrows in (a). (d) Lateral PFM phase image of the same area as (a). (e), (f) Variation of PFM phase as a function of the same film position as in (b) and (c), respectively. Scale bar is 10 μm.

Figures 3(b) and 3(c) are the plots of FFMI intensity vs. coordinates across DW1 (along ***x***//*b*), and across DW2 (along ***x***//*c*), respectively, the loci of which are indicated by the arrows in Fig. 3(a). It is clear that the change in the FFMI signal across DW2 is much more gradual with a large distance of 14 μm, than that across DW1 with a distance of about 1.5 μm. We

also observe that the width across DW2 depends on the thickness of the films, as presented in Fig. 4(a). The result clearly indicates that the orientation of DW2 should have a component extended parallel to the film surface: The observed gradual change in the FFMI intensity along the *c*-axis should be associated with the successive variation of the domain volume fraction as a function of the *c*-axis, because the FFMI intensity is averaged over the thickness direction.

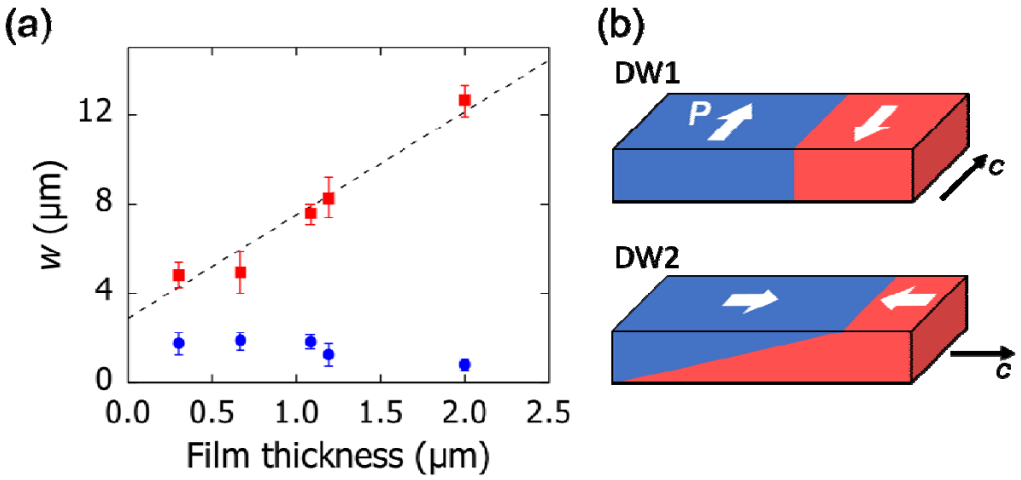

FIG. 4. Spatial width of domain walls as observed in the FFMI. (a) Film thickness dependence of spatial width (*w*) for the FFMI signal variation around DW1 (blue circles) and DW2 (red squares). Dashed line is a linear fit for the data of DW2. (b) Schematics for the orientations of DW1 (top) and DW2 (bottom) within the film. White arrows depict the horizontal component of spontaneous polarization.

Figure 3(d) shows a lateral PFM phase image, obtained for the same film as presented in Fig. 3(a). In contrast to the FFMI image, the PFM image (generally) exhibits a distinct variation in signal intensity at the domain boundary. For a comparison of FFMI and PFM, we also plotted the domain boundary obtained from the PFM image, as shown by the white curves in Fig. 3(a). Figures 3(e) and 3(f) are the plots of the PFM phase across DW1 and DW2, respectively, plotted in the same area as Fig. 3(b) and 3(c). We found that DW2 as observed by the PFM image coincides well with either edge of the gradual change in the

FFMI intensity. We also checked the consistency with the PFM amplitude image, as plotted in Supplementary Fig. S7 [28], confirming that similar features as the PFM phase image are observed. The most probable scenario on the observed difference between the FFMI image and the PFM image is the following: the PFM image should visualize the ferroelectric domains around the crystal surface, because the electric field applied between the tip and the electrode should be concentrated immediately beneath the tip, and sharply decays with the distance along the depth direction [33]. Moreover, the base electrode located at the side direction, as used in this study, should make the piezoresponse less sensitive to the depth direction compared to the case of the base electrode arranged at the bottom.

From the above observations, it is most probable that the gradual variation in FFMI signals indicates that DW2 should be considerably tilted from the axis perpendicular to the film surface, as schematically shown in Fig. 4(b), bottom. In other words, neighbouring ferroelectric domains with opposite polarization orientations overlap with each other in the thickness direction, in the case of DW2, eventually bringing a gradual change in the FFMI signals. In contrast, DW1 separates the ferroelectric domains by a plane that is roughly perpendicular to the film plane (Fig. 4(b) top). From the fitting slope for the plot in Fig. 4(a), DW2 should have a constant tilting angle of about 12° from the plane of the film/substrate interface. Note that the fitting slope of Fig. 4(a) also has a non-zero vertical intercept value at about 3 μm. This means that DW2 should involve a transition region between the neighbouring ferroelectric domains, where the magnitude of polarization gradually changes [21].

C. Origin of the marked orientation of ferroelectric domain walls

According to the recent first-principles calculations for the study compound, the polarization orientation is predicted to be tilted 10.6° from the *c*-axis within the *ac*-plane based on the calculation result of (a, b, c^*) = (0.08, 0, −7.51), which is roughly directed

toward the *c**-axis [11]. This means that the spontaneous polarization orientation should be slightly tilted from the film surface as presented in Fig. 5(a). Actually, we found from the vertical PFM measurements that the ferroelectric domains in Hdppz-Hca retain the vertical component of spontaneous polarization, as presented in Supplementary Fig. S8 [28].

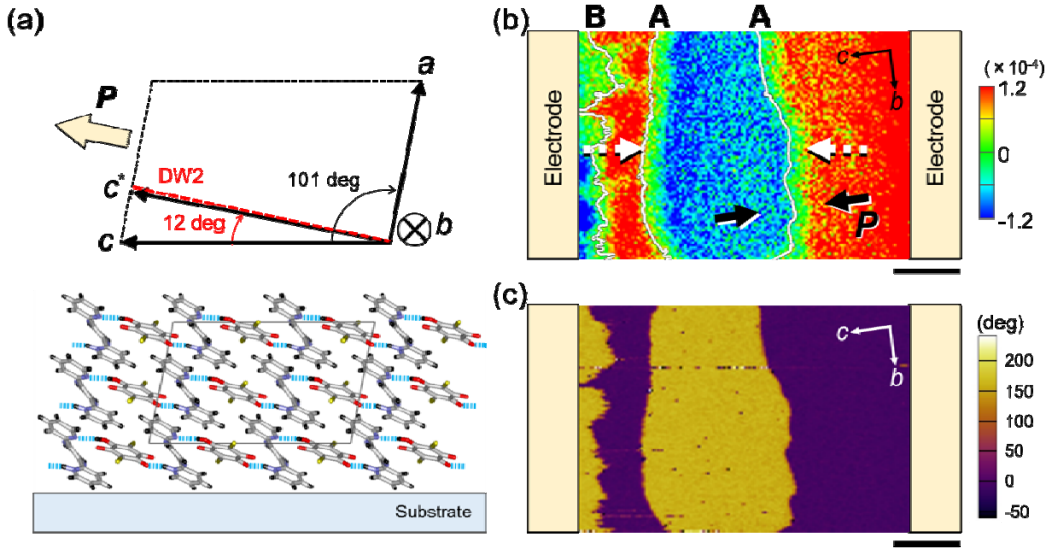

FIG. 5. Observed domain wall orientation and its relationship with crystallographic axes. (a) Crystallographic axes of Hdppz-Hca single-crystal film on a substrate. *b*- and *c*-axes are parallel to the substrate. (b) FFMI image and (c) Lateral PFM phase image of the same area of an Hdppz-Hca single-crystal film. White curves in (b) indicate the domain walls observed in (c). These domain walls stay at the locations after they are moved along the direction shown by the white dotted arrows in (b), respectively. Black arrows depict the horizontal component of spontaneous polarization. Scale bar is 10 μm.

To reveal the relationship between the orientation of DW2 and the crystal lattices, we investigated the crystallographic axes of the single-crystal films with non-inversion symmetry by means of thin-film x-ray diffraction measurements (see Supplementary Fig. S9 [28]). Figure 5(a) presents the crystallographic axes of the films: *b*- and *c*-axes are parallel to the substrate, whereas the *a*-axis is slightly tilted from the axis perpendicular to the substrate (the angle between the *a*-axis and *c*-axis is 101°). Note that the polarization reversal does not

cause any lattice deformation in Hdppz-Hca. This means that the direction of the *a*-axis is common to both ferroelectric domains with opposite polarization orientations.

Figures 5(b) and 5(c) show the FFMI image and the lateral PFM phase image measured for a film in which the *c*-axis points to the left and the *a*-axis tilts to the right in the figure. We determined the orientation of DW2 through a comparison between the FFMI and PFM images. The surface domain boundary is located at the left edge of the transition region in the FFMI image for a pair of DW2 located around the centre of the film (denoted as "A" in Fig. 5(b)). The result clearly shows that both DW2 are tilted downward to the right, and are roughly perpendicular to the *a*-axis. This indicates that the DW2 are roughly parallel to the bc^*-plane (see Fig. 5(a), top). We confirmed the observation of the same orientation relationships between DW2 and the crystallographic axes in other films (see Supplementary Fig. S10 [28]).

All the results presented above indicate that the DW2 should be the neutral domain walls that are parallel to the spontaneous polarization. This finding is in striking contrast to the naive assignment from the PFM measurements that the DW2 might be the charged domain walls. We should point out that the total area of DW2 is about five times larger than the case of domain walls perpendicular to the film surface, because of the tilt within the film. This feature may lead to the increase of interfacial energy, although suppression of the electrostatic energy derived from the bound charges must be more effective to minimize the free energy. We conclude that the orientation of DW2 should be stabilized to generate the substantial neutrality at the domain walls, by being directed along the spontaneous polarization.

Interestingly, we also noticed different orientations of domain walls in the film region close to the electrodes. For example, the domain wall denoted as "B" in Fig. 5(b) is tilted downward to the left, in reverse to the orientation of "A"-type DW2. In this case, it is clear that the domain wall should no longer be neutral, but be charged with bound charges. We consider that the electric field should be concentrated at around the edge of the electrodes,

which may modify the domain wall orientation. This feature illustrates the interface or extrinsic effects on the orientation and motion of the domain walls.

IV. CONCLUSIONS

We successfully visualized the structures and motions of ferroelectric domains and domain walls in single-crystal films of a proton-transfer-type ferroelectric molecular co-crystal of Hdppz-Hca, by means of a noncontact optical-probe technique that we call FFMI. By using the difference image sensing technique based on a CMOS area image sensor, we demonstrate that FFMI can sensitively, collectively, and quickly detect tiny changes in optical transmittance. We also demonstrate from the spectral analyses that the FFMI can sensitively probe the ferroelectric domain structures through the variation of proton positions under applied electric fields. Furthermore, the unique transmitted optical probe nature of the FFMI allow us to disclose three-dimensional domain wall structures in the depth direction through the combination with surface-sensitive PFM measurements. Analyses revealed the existence of two types of domain walls, denoted as DW1 and DW2. DW1 is a class of neutral domain walls that are parallel to the *ac*-plane and thus perpendicular to the film plane. In contrast, DW2 is another class of neutral domain walls that are parallel to the *bc**-plane, with a considerable tilt of about 78° from the axis perpendicular to the film plane. We conclude that the neutral domain walls with various types of orientational features should dominate the switching characteristics in ideal hydrogen-bonded ferroelectrics where the coupling of lattice elastic energy is negligible.

The FFMI technique as presented in this study is based on a unique and simple combination of the well-known first-order electro-optic effect and the cutting-edge image sensor technology. So the technique should be useful for many ferroelectric materials. As presented in this study, the technique is more advantageous to the PFM in that it can visualize

the ferroelectric domain structures over a wider area (about 100 times larger in the present study) and with shorter acquisition time (of several tens of times faster). These features should be useful for probing the topological nature of ferroelectric domain walls as well as the dynamics of domain-wall motion, and thus should open a new route for understanding and controlling the switchable electric dipoles as well as their pinning phenomena in ferroelectric materials.

ACKNOWLEDGMENTS

This work was partially supported by JSPS KAKENHI Grant Numbers JP16H02301 and JP16H05976, and also by JST CREST Grant Number JPMJCR18J2, Japan. The synchrotron X-ray study was performed with approval of the Photon Factory Program Advisory Committee (No. 2017S2-001). We thank Dr. Y. Noda for the technical instructions on PFM measurements. We thank Dr. S. Ishibashi for providing the calculation data of polarization orientation.

[1] W. J. Merz, Domain formation and domain wall motions in ferroelectric $BaTiO_3$ single crystals, Phys. Rev. **95,** 690-698 (1954).

[2] D. Damjanovic, Ferroelectric, dielectric and piezoelectric properties of ferroelectric thin films and ceramics, Rep. Prog. Phys. **61,** 1267–1324 (1998).

[3] C. T. Nelson, P. Gao, J. R. Jokisaari, C. Heikes, C. Adamo, A. Melville, S. Baek, C. M. Folkman, B. Winchester, Y. Gu, Y. Liu, K. Zhang, E. Wang, J. Li, L. Chen, C. Eom, D. G. Schlom, and X. Pan, Domain dynamics during ferroelectric switching, Science **334,** 968 – 971 (2011).

[4] L. He and D. Vanderbilt, First-principles study of oxygen-vacancy pinning of domain walls in $PbTiO_3$, Phys. Rev. B **68,** 134103 (2003).

[5] W. L. Warren, D. Dimos, G. E. Pike, B. A. Tuttle, M. V. Raymond, R. Ramesh, and J. T. Evans, Voltage shifts and imprint in ferroelectric capacitors, Appl. Phys. Lett. **67,** 866−868 (1995).

[6] G. Arlt, Twinning in ferroelectric and ferroelastic ceramics: stress relief, J. Mater. Sci. **25,** 2655–2666 (1990).

[7] W. Cao and L. E. Cross, Theory of tetragonal twin structures in ferroelectric perovskites with a first-order phase transition, Phys. Rev. B **44,** 5 (1991).

[8] S. Horiuchi, Y. Tokunaga, G. Giovannetti, S. Picozzi, H. Itoh, R. Shimano, Reiji Kumai, and Y. Tokura, Above-room-temperature ferroelectricity in a single-component molecular crystal, Nature **463,** 789–792 (2010).

[9] S. Horiuchi, F. Kagawa, K. Hatahara, K. Kobayashi, R. Kumai, Y. Murakami, and Y. Tokura, Above-room-temperature ferroelectricity and antiferroelectricity in benzimidazoles, Nat. Commun. **8,** 1308 (2012).

[10] S. Horiuchi, R. Kumai, and Y. Tokura, High-temperature and pressure-induced ferroelectricity in hydrogen-bonded supramolecular crystals of anilic acids and 2,3-Di(2-pyridinyl)pyrazine, J. Am. Chem. Soc. **135,** 4492 – 4500 (2013).

[11] K. Kobayashi, S. Horiuchi, S. Ishibashi, F. Kagawa, Y. Murakami, and R. Kumai, Structure–property relationship of supramolecular ferroelectric [H-66dmbp][Hca] accompanied by high polarization, competing structural phases, and polymorphs, Chem. Euro. J. **20,** 17515–17522 (2014).

[12] S. Horiuchi, K. Kobayashi, R. Kumai, and S. Ishibashi, Proton tautomerism for strong polarization switching, Nat. Commun. **8,** 14426 (2017).

[13] R. C. G. Naber, K. Asadi, P. W. M. Blom, D. M. de Leeuw, and B. de Boer, Organic nonvolatile memory devices based on ferroelectricity, Adv. Mater. **22,** 933–945 (2010).

[14] T. Furukawa, Ferroelectric properties of vinylidene fluoride copolymers, Phase Trans. **18,** 143–211 (1989).

[15] S. Horiuchi and Y. Tokura, Organic ferroelectrics, Nat. Mater. **7,** 357 - 366 (2008).

[16] Y. Noda, T. Yamada, K. Kobayashi, R. Kumai, S. Horiuchi, F. Kagawa, and T. Hasegawa, Few-volt operation of printed organic ferroelectric capacitor, Adv. Mater. **27,** 6475 - 6481 (2015).

[17] A. Gruverman, O. Auciello, and H. Tokumoto, Imaging and control of domain structures in ferroelectric thin films via scanning force microscopy, Annu. Rev. Mater. Sci. **28,** 101–23 (1998).

[18] F. Kagawa, S. Horiuchi, N. Minami, S. Ishibashi, K. Kobayashi, R. Kumai, Y. Murakami, and Y. Tokura, Polarization switching ability dependent on multidomain topology in a uniaxial organic ferroelectric, Nano Lett. **14,** 239 - 243 (2014).

[19] Y. Cho, A. Kirihara, and T. Saeki, Scanning nonlinear dielectric microscope, Review of Scientific Instruments **67,** 2297 (1996).

[20] C. Gao, F. Duewer, Y. Lu, and X.-D. Xiang, Quantitative nonlinear dielectric microscopy of periodically polarized ferroelectric domains, Appl. Phys. Lett. **73,** 1146 (1998).

[21] Y. Uesu, S. Kurimura, and Y. Yamamoto, Optical second harmonic images of 90° domain structure in $BaTiO_3$ and periodically inverted antiparallel domains in $LiTaO_3$, Appl. Phys. Lett. **66,** 2165 (1995).

[22] M. Fiebig, V. V. Pavlov, and R. V. Pisarev, Second-harmonic generation as a tool for studying electronic and magnetic structures of crystals: review, J. Opt. Soc. Am. B **22,** 96-118 (2005).

[23] M. Sotome, N. Kida, S. Horiuchi, and H. Okamoto, Visualization of ferroelectric domains in a hydrogen-bonded molecular crystal using emission of terahertz radiation, Appl. Phys. Lett. **105,** 041101 (2014).

[24] M. Sotome, N. Kida, S. Horiuchi, and H. Okamoto, Terahertz radiation imaging of ferroelectric domain topography in room-temperature hydrogen-bonded supramolecular ferroelectrics, ACS Photonics **2,** 1373 – 1383 (2015).

[25] H. Kishida, H. Takamatsu, K. Fujinuma, and H. Okamoto, Ferroelectric nature and real-space observations of domain motions in the organic charge-transfer compound tetrathiafulvalene-*p*-chloranil, Phys. Rev. B **80,** 205201 (2009).

[26] R. Kumai, S. Horiuchi, Y. Okimoto, and Y. Tokura, Large dielectric susceptibility associated with proton transfer in a supramolecular structure of chloranilic acid and 5, 5'-dimethyl-2, 2'-bipyridine, J. Chem. Phys. **125,** 084715 (2006).

[27] M. K. Nazeeruddin and K. Kalyanasundaram, Acid-base behavior in the ground and excited states of ruthenium (II) complexes containing tetraimines or dicarboxybipyridines as protonatable ligands, Inorg. Chem. **28,** 4251-4259 (1989).

[28] See Supplemental Material at [URL] for optical micrographs of a single-crystal thin film of Hdppz-Hca. The Supplemental Material also contains detail information of FFMI, PFM and x-ray diffraction.

[29] J. Tsutsumi, S. Matsuoka, T. Yamada, and T. Hasegawa, Gate-modulation imaging of organic thin-film transistor arrays: Visualization of distributed mobility and dead pixels, Org. Electron. **25,** 289–294 (2015).

[30] V. Janovec, On the theory of the coercive field of single-domain crystals of $BaTiO_3$, Czech. J. Phys. **8,** 3 – 15 (1958).

[31] M. Dawber, P. Chandra, P. B. Littlewood, and J. F. Scott, Depolarization corrections to the coercive field in thin-film ferroelectrics, J. Phys.: Condens. Matter **15,** L393 – L398 (2003).

[32] N. A. Pertsev, J. Rodríguez Contreras, V. G. Kukhar, B. Hermanns, H. Kohlstedt, and R. Waser, Coercive field of ultrathin $Pb(Zr_{0.52}Ti_{0.48})O_3$ epitaxial films, Appl. Phys. Lett. **83,** 3356 (2003).

[33] T. Jungk, Á. Hoffmann, and E. Soergel, Impact of the tip radius on the lateral resolution in piezoresponse force microscopy, New. J. Phys. **10,** 013019 (2008).